Journal of Sound and Vibration 484 (2020) 115521

Contents lists available at ScienceDirect

Journal of Sound and Vibration

journal homepage: www.elsevier.com/locate/jsvi

Parametric study and shape optimization of Piezoelectric Energy Harvesters by isogeometric analysis and kriging metamodeling

P. Peralta [a,b], R.O. Ruiz [c,*], S. Natarajan [d], E. Atroshchenko [b]

[a] Department of Mechanical Engineering, Universidad de Chile, Av. Beauchef 851, Santiago, Chile
[b] School of Civil and Environmental Engineering, University of New South Wales, Sydney, Australia
[c] Department of Civil Engineering, Universidad de Chile, Av. Blanco Encalada 2002, Santiago,Chile
[d] Department of Mechanical Engineering, Indian Institute of Technology, Madras, India

ARTICLE INFO

Article history:
Received 29 November 2019
Revised 11 June 2020
Accepted 12 June 2020
Available online 20 June 2020
Handling Editor: J Cheer

Keywords:
Piezoelectric energy harvester
Parametric study
Kirchhoff-love plates
Isogeometric analysis
Shape optimization

ABSTRACT

Piezo-electric energy harvesters (PEHs) are widely used to recycle waste vibrations for powering small electronic devices. In this work, the performance of PEHs of non-conventional shapes is studied with the aim to optimize their design. A PEH is modeled as a bimorph cantilever Kirchhoff-Love plate subjected to base acceleration. The shape is described by Non Uniform Rational B-Splines (NURBS), and the problem is solved by the isogeometric analysis (IGA). Accuracy of the IGA solutions is demonstrated on two benchmark problems. Then, we conduct a parametric study to investigate the effect of shape perturbations on the fundamental frequency, the peak amplitude of the frequency response function (FRF) and the peak amplitude of the FRF per unit of area. Next, we build the Kriging meta-model to obtain the boundary shapes that maximize the peak amplitude of the FRF and the peak amplitude of the FRF per unit of area for a target frequency. The optimization is performed for three cases: with a fixed tip mass, without a tip mass and with a tip mass being one of the design parameters.

1. Introduction

Vibration energy harvesting is a process of converting the wasted mechanical energy into electric power, which can be used to power small electronic devices or stored for future use. It is a promising technology, emerging as an alternative to the use of standard chemical batteries, particularly in applications where battery replacement is difficult, expensive or unfeasible (e.g. remote sensors). Piezoelectric transduction mechanism is one of the common and the most efficient energy conversion methods, which utilizes the ability of piezoelectric materials to develop electric charge from applied elastic strain.

In this study, we focus on a cantilever-type piezoelectric harvester (PEH), mounted on a vibrating base. This configuration (usually with a mass placed on the free end) has been studied extensively, both experimentally and analytically, due to its two main advantages: low resonance frequency and high strain for a given force [1]. A number of models have been proposed in the literature. The earliest and the simplest one is the so-called Single Degree of Freedom (SDOF) model [2], where the vibration energy harvesting system is described by a second-order differential equation with lumped parameters (i.e. equivalent mass, stiffness and damping), coupled with the electrical circuit equation through the piezo-electric constitutive law [3,4]. Due to its

* Corresponding author.
E-mail address: rafaelruiz@uchile.cl (R.O. Ruiz).

https://doi.org/10.1016/j.jsv.2020.115521
0022-460X/

simplicity, the SDOF model is widely used in the literature [5], however, as shown in Refs. [6], its accuracy deteriorates for low tip mass to beam mass ratios. Correction factors were derived in Ref. [6], where a more sophisticated model, based on the Euler-Bernoulli beam theory was also introduced. The approach, often referred to as a distributed parameter electro-mechanically coupled model, was further developed in Ref. [7] and validated by experiments in Ref. [8]. However, PEHs are typically designed and manufactured as thin structures more similar to plates than beams. In this direction, De Marqui et al. [9] proposed the electro-mechanical model based on the Kirchhoff-Love plate theory, subsequently discretized by the finite element method. The accuracy of the model was demonstrated in comparison with the analytical solution for the beam and the experimental data. The same formulation is adopted in the present work in conjunction with the isogeometric analysis (IGA).

Three main directions are pursued in PEHs' performance optimization: improving circuit properties, designing new materials and optimizing the shape of a device. As early as in 2005, first studies appeared indicating that a rectangular beam does not yield a maximum possible output power due to uneven strain distribution. Roundy in Ref. [10] compared the beams of rectangular and trapezoidal shapes in terms of bending energy generated due to the force applied at the tip, and showed that trapezoidal shapes (widening at the fixed end) can yield more than twice the energy per unit of volume. Two PEHs models based on rectangular and trapezoidal cantilevers were compared in Ref. [11], where an improvement of 30% in power output for the same volume, tip mass and natural frequency was reported for a trapezoidal shape. Rectangular, trapezoidal and triangular shapes were also compared in Ref. [12], trapezoidal and reverse trapezoidal (widening at the free end) in Ref. [13]. Goldschmidtboeing et al. in Ref. [14] examined a parameterized family of trapezoids, varying from rectangular to triangular shapes, and arrived to the conclusion that the optimal configuration is a triangular shape with a high ratio of the tip mass to the beam mass. In Ref. [15] shape optimization is carried out over a family of polynomial shapes and the effect of tip mass to beam mass ratio is discussed. In Ref. [16] it was reported that quadratic polynomial shaped beams can double the amount of energy produced by rectangular shaped PEHs. Beams of varying thickness were studied in Ref. [17], where FEM model combined with genetic algorithm was used to find an optimal design. V-shape beams were studied in Ref. [18].

It can be noted, that all research on PEHs of non-rectangular shapes has been limited to a) employing a simple model (SDOF or a beam) and b) considering narrow design space (linear or lower-degree polynomial shapes). The analysis framework developed in the present work overcomes both these limitations. First, the model is based on the Kirchhoff-Love plate theory and highly accurate solutions are obtained by the IGA. Second, the design of a PEH is described by the varying width, length and positions of the control points along the boundary, which describe the boundary shape. In the results, presented in chapters 4 and 5, two sides of the device were considered symmetric, however, this assumption can also be weakened. Finally, optimization was performed by using the Kriging metamodel to build a massive database of different geometries and using a blind search approach to identify geometries with optimal performance. Although the approach involves an important computational burden (in particular to train the metamodel and fill the database), it was chosen due to its ability to find multiple solutions simultaneously. Furthermore, after the generation of the database, the optimization could be constrained for specific fundamental frequencies with no additional computational cost. Optimization objectives are set as the peak value of the Frequency Response Function (FRF) and the peak value of FRF per unit of area. A family of optimal designs is obtained through a Pareto front. Three design configurations are considered: without tip mass, with a specific tip mass and with variable tip mass (which is included in optimization as one of the design parameters).

Respect to the use of an IGA based method, it is important to highlight the following details. Isogeometric analysis is a variation of the finite element method, in which polynomial basis functions are replaced by Non-Uniform Rational B-Splines (NURBS) [19]. IGA is chosen as a numerical tool in this work due to the following two advantages. First, higher degree and higher continuity of NURBS basis functions make them suitable for problems described by higher order partial differential equations. Weak form of the Kirchhoff-Love plate problem involves derivatives of second order and therefore requires shape functions of C^1-continuity. The plate geometry in this work is a one-patch domain, and knot insertion and degree elevation ($h-$ and $p-$ refinement) can be done with preserving highest continuity (C^{p-1}) of NURBS. Examples of IGA for Kirchhoff-Love plates and shells can be found in Ref. [20–22]. Second, IGA allows a convenient uniform description of the design and analysis models, without the need to fit the mesh to the boundary geometry. In the design model, the boundary geometry is described by the varying control points and during the shape optimization procedure multiple locations are tested. After the control points are chosen, the corresponding geometry is further refined to obtain a set of basis functions for the solution approximation in the analysis model (generalization of the IGA, that allows independent representation of the geometry and the solution was proposed in Ref. [23] and can also be used for analysis in this work). Examples of IGA-based shape optimization are given in Refs. [24–27], recent review is given in Ref. [28].

Ultimately, fast, accurate and versatile numerical models are an important tool for development of methods of PEHs' performance enhancement. With the model, developed in this study, it takes less than 1 s to obtain the FRF with error less than one percent. In order to perform shape optimization, we evaluated the model 30.000 times for different sample geometries to build the Kriging metamodel. Once the kriging is trained it is used to generate a massive database with 2.000.000 of different geometries. The total time required to train the metamodel and to generate the database is about 20 h on a 20 core PC (process that is performed only once). After, a blind search approach is adopted to perform the optimization. Here, any new optimization with any new constrain is performed in a lapse of a few seconds.

The model, developed in this work, can be used in other studies, such as for example, the impact of uncertainties on the behaviour of PEHs [29–31]. Current studies are limited to simple beam geometries and having a model, capable to describe devices of different shapes with high efficiency and accuracy, can significantly extend the analysis space. Model can be also cou-

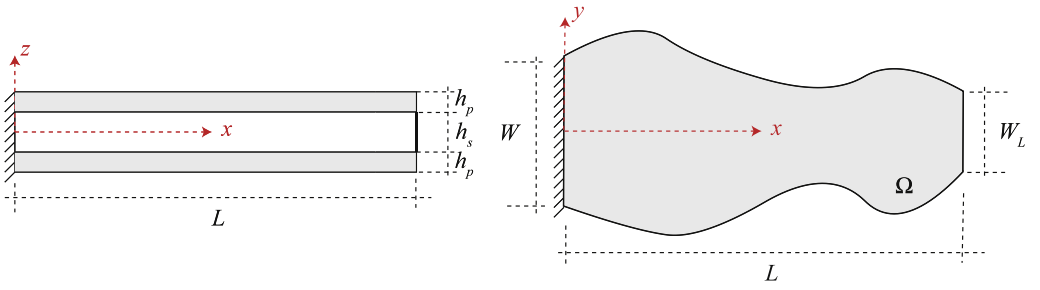

Fig. 1. Scheme of the bimorph piezoelectric energy harvester with an arbitrary shape, modeled as a cantilever plate, consisting of two piezoelectric patches and one substructure layer.

pled with other applications, such as fluid-structure interaction based PEHs [32] or human-based PEHs [33] (a comprehensive review of PEH mechanisms is given in Ref. [34]).

The remainder of the paper is organized as follows. The theoretical framework of the model is presented in Section 2. In Section 3, numerical results are verified against the data from the literature. In order to understand the impact of the size and shape in the response of the devices, a parametric study is carried out in Section 4. Finally, shape optimization is employed in Section 5 to show the potential of the method in the design process to generate devices with optimal shapes. Conclusions are presented in Section 6.

2. PEH modeling based on Kirchhoff-Love plate theory

The PEH is modeled as a cantilever plate composed of a main structural layer (substructure) with two layers of piezoelectric material bonded to its upper and lower faces (configuration known as bimorph). A general scheme of these devices is presented in Fig. 1 where it is possible to observe a lateral and an upper views. It is assumed, that all layers occupy domain Ω in $x-y$ plane and have uniform thickness (h_s and h_p denote the thickness of the substructural and piezoelectric layers, respectively). Then, the total thickness of the PEH is $h = h_s + 2h_p$. The 3D domain of the substructure layer is denoted as $V_s = \Omega \times [-\frac{h_s}{2}, \frac{h_s}{2}]$, two piezoelectric layers occupy domain $V_s = \Omega \times \left([-\frac{h}{2}, \frac{-h_s}{2}] \cup [\frac{h_s}{2}, \frac{h}{2}]\right)$. In the most general case, Ω can be of arbitrary shape, however, in this study we limit our attention to configurations, which consist of two straight parallel sides of width W (fixed edge) and W_L (free edge), as shown in Fig. 1(b). The length of the device is denoted by L (see Fig. 1).

In what follows, we will also need the material parameters: ρ_s is the substructural density and ρ_p is the piezoelectric layer density. The total mass of the device is then defined as $m = \int_{V_p} \rho_p dV_p + \int_{V_s} \rho_s dV_s$. Area of Ω is denoted as S ($S = \int_\Omega d\Omega$), the total volume of the PEH is denoted by V ($V = \int_{V_p} dV_p + \int_{V_s} dV_s$).

According to the Kirchhoff-Love plate theory, the total displacement field $\boldsymbol{u} = \boldsymbol{u}(x, y, z, t) = (u, v, w)^T$ is defined as:

$$\boldsymbol{u} = \left\{ -z\frac{\partial}{\partial x}, -z\frac{\partial}{\partial y}, 1 \right\}^T w, \tag{1}$$

where $w = w(x, y, t)$ is the unknown transverse deflection of the neutral plane, which in this case corresponds to the middle section of the plate ($z = 0$) due to the symmetric arrangement of the layers. The corresponding mechanical strain components $\{\varepsilon_x, \varepsilon_y, \varepsilon_{xy}\}^T$ can be subsequently expressed as

$$\mathbf{S} = \{\varepsilon_x, \varepsilon_y, 2\varepsilon_{xy}\}^T = -z\left\{ \frac{\partial^2}{\partial x^2}, \frac{\partial^2}{\partial y^2}, 2\frac{\partial^2}{\partial x \partial y} \right\}^T w \tag{2}$$

The substructure layer is considered as an isotropic homogeneous material with Young's modulus E_S and Poisson's ratio ν_S. Under the plane-stress conditions, the following constitutive relation holds:

$$\begin{Bmatrix} \sigma_x \\ \sigma_y \\ \sigma_{xy} \end{Bmatrix} = \frac{E_S}{1-\nu_S^2} \begin{bmatrix} 1 & \nu_S & 0 \\ \nu_S & 1 & 0 \\ 0 & 0 & \frac{1-\nu_S}{2} \end{bmatrix} \begin{Bmatrix} \varepsilon_x \\ \varepsilon_y \\ 2\varepsilon_{xy} \end{Bmatrix}, \tag{3}$$

which can be written in a compact notation as

$$\mathbf{T} = \mathbf{c_s}\mathbf{S}, \tag{4}$$

where

$$\mathbf{T} = \{\sigma_x, \sigma_y, \sigma_{xy}\}^T, \qquad \mathbf{c_s} = \frac{E_S}{1-\nu_S^2}\begin{bmatrix} 1 & \nu_S & 0 \\ \nu_S & 1 & 0 \\ 0 & 0 & \frac{1-\nu_S}{2} \end{bmatrix}. \tag{5}$$

On the other hand, the constitutive equations for the piezoelectric layers are written as [35].

$$\begin{Bmatrix} \mathbf{T} \\ \mathbf{D} \end{Bmatrix} = \begin{bmatrix} \mathbf{c}_p^E & -\mathbf{e}^T \\ \mathbf{e} & \boldsymbol{\varepsilon}^S \end{bmatrix} \begin{Bmatrix} \mathbf{S} \\ \mathbf{E} \end{Bmatrix} \tag{6}$$

Under assumption that the layer is poled in the z-direction, the vector of electric displacement components ($\mathbf{D}$) and the vector of electric field components ($\mathbf{E}$) have only one non-zero component leading to

$$\mathbf{D} = D_z, \;\; \mathbf{E} = E_z \tag{7}$$

while the plain-stress condition in the piezoelectric layer leads to

$$\mathbf{c}_p^E = \begin{bmatrix} \overline{c}_{11}^E & \overline{c}_{11}^E & 0 \\ \overline{c}_{12}^E & \overline{c}_{22}^E & 0 \\ 0 & 0 & \overline{c}_{66}^E \end{bmatrix}, \;\; \mathbf{e} = \{\overline{e}_{31}, \overline{e}_{32}, 0\}, \;\; \boldsymbol{\varepsilon}^S = \overline{\varepsilon}_{33}^S \tag{8}$$

Based on the Hamilton's principle, the weak form of the problem is given as [36].

$$\begin{aligned} \int_{t_1}^{t_2} \Bigg\{ & \int_{V_s} \rho_s \delta\dot{\mathbf{u}}^T \dot{\mathbf{u}} dV_s + \int_{V_p} \rho_p \delta\dot{\mathbf{u}}^T \dot{\mathbf{u}} d\Omega_p + \sum_{i=1}^{n_m} \delta\dot{\mathbf{u}}^T(x_i, y_i, t)\, \dot{\mathbf{u}}(x_i, y_i, t)\, m_i - \int_{V_s} \delta\mathbf{S}^T \mathbf{c}_s \mathbf{S} dV_s - \\ & \int_{V_p} \delta\mathbf{S}^T \mathbf{c}_p^E \mathbf{S} dV_p + \int_{V_p} \delta\mathbf{S}^T \mathbf{e}^T \mathbf{E} dV_p + \int_{V_p} \delta\mathbf{E}^T \mathbf{e}\mathbf{S} dV_p + \int_{V_p} \delta\mathbf{E}^T \boldsymbol{\varepsilon}^S \mathbf{E} dV_p + \\ & \sum_{j=1}^{n_f} \delta\mathbf{u}^T(x_j, y_j, t)\mathbf{f}_j + \sum_{k=1}^{n_q} \delta\phi(x_k, y_k, t)\, q(x_k, y_k, t) \Bigg\} dt = 0 \end{aligned} \tag{9}$$

In Eq. (9), a set of point masses $\{m_i, i = 1 \dots n_m\}$ located at (x_i, y_i), a set of discrete mechanical forces $\{\mathbf{f}_j, j = 1 \dots n_f\}$ applied at (x_j, y_j) and discrete electric charge outputs q extracted at (x_k, y_k) are added to the system, while ϕ is the scalar electrical potential.

In eq. (9), the first three terms correspond to the variation of the kinetic energy as a contribution of the substructural and piezoelectric layers together with the point masses m_i. The fourth term corresponds to the variation of the elastic potential energy of the substructure layer. The fifth and sixth terms correspond to the variation of the elastic potential energy of the piezoelectric layers, where an electro-mechanical coupling term appears. The seventh and eighth terms corresponds to the variation of the electrical potential energy, where again an electro-mechanical term appears. Finally, the last three terms correspond to the variation of the non conservative work due to distributed and concentrated loads applied in the surface of the device (tenth and eleventh terms, respectively), while the last term corresponds to the electrical work extracted.

Some assumptions, common for this kind of problems, are adopted: (*a*) the boundary between the piezoelectric layers and the substructure is perfect, (*b*) the piezoelectric layers are covered by continuous electrodes, (*c*) the electrodes are perfectly conductive and have negligible thickness, (*d*) in order to estimate the generated power, a resistive electrical load R_l is considered in the electric domain [9], (*e*) the voltage generated in the system is constant, and it is denoted by v_p and (*f*) the electric field, is uniform in the z-direction, i.e.

$$E_z = -\frac{\partial\phi}{\partial z} = -\frac{v_p}{h_p} \tag{10}$$

2.1. Non-Uniform Rational B-Splines (NURBS)

In this section we give a brief overview of B-Splines and NURBS basis functions [37], which will be used to discretize Eq. (9) according to principles of IGA. B-Splines are piece-wise polynomials defined on a so-called knot vector. The knot vector is a non-decreasing sequence of $n + p + 1$ real numbers ξ_i (knots):

$$\Sigma = \{\xi_1 = 0, \xi_2, \dots, \xi_{n+p+1} = 1\}, \tag{11}$$

where n is the number of basis functions and p is the degree. B-Spline basis functions are defined recursively as

$$N_i^0(\xi) = \begin{cases} 1 & \text{if } \xi_i \le \xi < \xi_{i+1} \\ 0 & \text{otherwise} \end{cases} \tag{12}$$

and

$$N_i^p(\xi) = \frac{\xi - \xi_i}{\xi_{i+p} - \xi_i} N_i^{p-1}(\xi) + \frac{\xi_{i+p+1} - \xi}{\xi_{i+p+1} - \xi_{i+1}} N_{i+1}^{p-1}(\xi), \qquad p = 1, 2, 3, \ldots \tag{13}$$

The Non-Uniform Rational B-Splines (NURBS) are defined as:

$$R_i^p(\xi) = \frac{N_i^p(\xi)\overline{w}_i}{\sum_{j=1}^n N_j^p(\xi)\overline{w}_j}, \tag{14}$$

where $\overline{w}_i$ are the weights. Note that weights are denoted here with a bar to avoid confusion with the plate deflection. When all weights are equal, NURBS reduce to B-Splines.

A NURBS curve is defined using a set of NURBS basis functions and a set of n control points $\mathbf{P}_i$:

$$\mathbf{C}(\xi) = \sum_{i=1}^{n} R_i^p(\xi)\mathbf{P}_i, \qquad \xi \in [0, 1] \tag{15}$$

Two-dimensional NURBS basis is defined by the tensor product of two one-dimensional NURBS bases, i.e.

$$R_{i,j}^{p,q}(\xi, \eta) = \frac{N_i^p(\xi)N_i^q(\eta)\overline{w}_{i,j}}{\sum_{\widehat{i}=1}^n \sum_{\widehat{j}=1}^m N_{\widehat{i}}^p(\xi)N_{\widehat{j}}^q(\eta)\overline{w}_{\widehat{i},\widehat{j}}}, \tag{16}$$

where $N_j^q(\eta)$ are NURBS of degree q defined on knot vector $\Pi = \{\eta_0 = 0, \eta_1, \ldots \eta_{m+q+1} = 1\}$.

Then, a two-dimensional NURBS surface is defined as

$$\mathbf{S}(\xi, \eta) = \sum_{i=1}^{n}\sum_{j=1}^{m} R_{i,j}^{p,q}(\xi, \eta)\mathbf{P}_{i,j} \qquad (\xi, \eta) \in [0, 1] \times [0, 1] \tag{17}$$

where $\mathbf{P}_{i,j}$ is a set of $n \times m$ control points with weights $\overline{w}_{i,j}$. In what follows, we use the notation:

$$N_I(\boldsymbol{\xi}) = R_{i,j}^{p,q}(\xi, \eta), \tag{18}$$

where $\boldsymbol{\xi} = (\xi, \eta)$ defines the parametric coordinate ($\boldsymbol{\xi} \in [0, 1] \times [0, 1]$) and $I = (i, j)$ is a two-dimensional index ($I = 1..k, k = n \times m$). Eq. (17) defines a map between the physical space $\mathbf{x} = (x, y) \in \Omega$ and the parameter space $\boldsymbol{\xi} \in [0, 1] \times [0, 1]$:

$$\mathbf{x}(\boldsymbol{\xi}) = \sum_{I=1}^{k} N_I(\boldsymbol{\xi})\widetilde{\mathbf{x}}_I, \tag{19}$$

where $\widetilde{\mathbf{x}}_I = \mathbf{P}_{i,j}$.

2.2. Isogeometric analysis

According to provisions of the isogeometric analysis, the unknown displacement w is approximated using the basis functions $N_I(\boldsymbol{\xi})$, i.e.

$$w(\boldsymbol{\xi}, t) = \sum_{I=1}^{k} N_I(\boldsymbol{\xi})w_I(t), \tag{20}$$

where $w_I(t)$ are the so-called control variables (i.e. the deflection projected at control point I). Eq. (20) together with the mapping (19) is then used to define $\boldsymbol{u}$ according to Eq. (1) and discretize Eq. (9).

In particular, the first three terms in eq. (9) constitute the mass matrix $\mathbf{M} \in \mathbb{R}^{k \times k}$. Note, that this matrix accounts for the mass of the layers (substructure and piezoelectric layers) and n_m point masses m_i added to positions (x_i, y_i) in Ω.

$$\begin{aligned} M_{IJ} = &\int_{V_s} \rho_s \left(N_I N_J + z^2 N_{I,x} N_{J,x} + z^2 N_{I,y} N_{J,y}\right) dV_s + \\ &\int_{V_p} \rho_p \left(N_I N_J + z^2 N_{I,x} N_{J,x} + z^2 N_{I,y} N_{J,y}\right) dV_p + \\ &\sum_{i=1}^{n_m} N_I(x_i, y_i) N_J(x_i, y_i)\, m_i \end{aligned} \tag{21}$$

After integrating the first two terms with respect to z, Eq. (21) can be reduced to

$$M_{IJ} = (\rho_s h_s + 2\rho_p h_p)\int_\Omega N_I N_J d\Omega + \left(\rho_s \frac{h_s^3}{12} + \rho_p \frac{h_p}{6}\left(4h_p^2 + 6h_p h_s + 3h_s^2\right)\right) \int_\Omega (N_{I,x}N_{J,x} + N_{I,y}N_{J,y})d\Omega + \sum_{i=1}^{n_m} N_I(x_i, y_i)N_J(x_i, y_i)\, m_i \tag{22}$$

The stiffness matrix $\mathbf{K} \in \mathbb{R}^{k\times k}$ is derived from the fourth and fifth terms in Eq. (9) with components

$$\begin{aligned} K_{IJ} &= \int_{V_s} z^2 \mathbf{B}_I^T \mathbf{c}_s \mathbf{B}_J dV_s + \int_{V_p} z^2 \mathbf{B}_I^T \mathbf{c}_p^E \mathbf{B}_J dV_p \\ &= \frac{h_s^3}{12}\int_\Omega \mathbf{B}_I^T \mathbf{c}_s \mathbf{B}_J d\Omega + \frac{h_p}{6}\left(4h_p^2 + 6h_p h_s + 3h_s^2\right)\int_\Omega \mathbf{B}_I^T \mathbf{c}_p^E \mathbf{B}_J d\Omega \end{aligned} \tag{23}$$

where

$$\mathbf{B}_I = \left\{-N_{I,xx} \quad -N_{I,yy} \quad -2N_{I,xy}\right\}^T \tag{24}$$

The sixth term in Eq. (9) introduces an electro-mechanical coupling which can be expanded employing Eqs. (2), (7) and (8) as:

$$\int_{V_p} \delta \mathbf{S}^T \mathbf{e}^T \mathbf{E} dV_p = \delta \int_{V_p} -z\left(\frac{\partial^2 w}{\partial x^2}\overline{e}_{31} + \frac{\partial^2 w}{\partial y^2}\overline{e}_{32}\right) E_z dV_p \tag{25}$$

From the assumption that the electrical field is uniform in the z-direction (Eq. (10)), the previous equation can be expressed as:

$$\int_{V_p} \delta \mathbf{S}^T \mathbf{e}^T \mathbf{E} dV_p = -\delta \int_{V_p} \frac{z}{h_p}\left(\frac{\partial^2 w}{\partial x^2}\overline{e}_{31} + \frac{\partial^2 w}{\partial y^2}\overline{e}_{32}\right) v_p dV_p \tag{26}$$

where the electrical potential varies linearly through the thickness (see for instance Ref. [9]). Finally, using the NURBS approximation for the displacements (Eq. (20)), an electro-mechanical coupling vector $\mathbf{\Theta} \in \mathbb{R}^{k\times 1}$ is introduced as

$$\Theta_I = \int_{V_p} \frac{z}{h_p}\left(\overline{e}_{31}N_{I,xx} + \overline{e}_{32}N_{I,yy}\right) dV_p \tag{27}$$

which after through-thickness integration takes the following form:

$$\Theta_I = (h_p + h_s)\int_\Omega \left(\overline{e}_{31}N_{I,xx} + \overline{e}_{32}N_{I,yy}\right) d\Omega \tag{28}$$

Based on the definitions introduced in Eqs. (22), (23) and (27), it is possible to establish the mechanical equation of motion as:

$$\mathbf{M}\ddot{\mathbf{w}} + \mathbf{C}\dot{\mathbf{w}} + \mathbf{K}\mathbf{w} - \mathbf{\Theta} v_p = \mathbf{F} \tag{29}$$

where $\mathbf{w} \in \mathbb{R}^{k\times 1}$ is a vector of $w_I(t)$ and

$$\mathbf{C} = \alpha_o \mathbf{M} + \beta_o \mathbf{K} \tag{30}$$

is the mechanical damping matrix ($\mathbf{C} \in \mathbb{R}^{k\times k}$) assuming a proportional damping, where the coefficients α_o and β_o are usually tuned to match specific damping ratios for the first two vibrational modes.

The right hand side of Eq. (29) is the distributed force $\mathbf{F} \in \mathbb{R}^{k\times 1}$, which represents inertial effect due to the transverse acceleration of the base:

$$\mathbf{F} = -\mathbf{M}\ddot{\mathbf{Y}}, \tag{31}$$

where vector $\ddot{\mathbf{Y}}$ contains the accelerations of all control points in the mesh, which in this case is equal to the base acceleration a_b, i.e. $\ddot{\mathbf{Y}} = a_b(1, 1, 1, \ldots)^T$. Using the partition of unity property of NURBS, Eq. (31) can be simplified to:

$$\begin{aligned} \mathbf{F}_I = -a_b \Bigg\{ & (\rho_s h_s + 2\rho_p h_p)\int_\Omega N_I d\Omega \\ & + \left(\rho_s \frac{h_s^3}{12} + \rho_p \frac{h_p}{6}\left(4h_p^2 + 6h_p h_s + 3h_s^2\right)\right)\sum_{J=1}^{k}\int_\Omega (N_{I,x}N_{J,x} + N_{I,y}N_{J,y})d\Omega \\ & + \sum_{i=1}^{n_m} N_I(x_i, y_i)\, m_i \Bigg\} \end{aligned}$$

In what follows we will use the notation: $\mathbf{F} = -a_b\mathbf{r}$, where the definition of vector $\mathbf{r}$ follows directly from Eq. (32).

On the other hand, the seventh, eighth and the last term of Eq. (9) lead to another coupled equation associated with the electrical balance. The seventh term yields coupling component $\boldsymbol{\Theta}^T\mathbf{w}$. The eighth term of Eq. (9) together with Eq. (10) defines the capacitance $C_p \in \mathbb{R}$ as

$$C_p = \int_{V_p} \frac{\overline{\varepsilon}^S_{33}}{h_p^2} dV_p = 2S\frac{\overline{\varepsilon}^S_{33}}{h_p} \tag{33}$$

while the last term in Eq. (9) defines the total electrical charge output Q. This balance leads to the following companion equation for Eq. (29)

$$C_p v_p + Q + \boldsymbol{\Theta}^T\mathbf{w} = 0 \tag{34}$$

If time derivative of Eq. (34) is taken, the load boundary condition $\dot{Q} = v_p/R_l$ due to the electrical shunt resistance R_l can be introduced as:

$$C_p\dot{v}_p + \frac{v_p}{R_l} + \boldsymbol{\Theta}^T\dot{\mathbf{w}} = 0 \tag{35}$$

Finally, Eq. (29) and Eq. (35) form a set of governing electro-mechanical equations of the PEH. It is important to note that on a bimorph configuration, the piezoelectric layers could be connected in series or in parallel. In particular, the connection has an impact on the integration of the electro-mechanical coupling vector (Eq. (27)) and the integration of the capacitance (Eq. (33)). The results presented in equations (27) and (33) correspond to the parallel connection. In the case of the series connection, the electro-mechanical coupling vector takes the value of a single piezoelectric layer. On the other hand, the value of the capacitance is 0.5 times the result of a single piezoelectric layer.

Considering that the base acceleration in the transversal direction is a harmonic motion of the form $a_b = A_B e^{j\omega t}$, it is possible to define the output voltage as $v_P = V_P e^{j\omega t}$ (where $j = \sqrt{-1}$). Next, the Frequency Response Function (FRF) that relates the output voltage $V_p = V_P(\omega)$ and the base acceleration $A_B = A_B(\omega)$ (for excitation frequency ω), is derived from Eqs. (29) and (35) as:

$$\frac{V_P(\omega)}{A_B(\omega)} = j\omega\left(\frac{1}{R_l} + j\omega C_p\right)^{-1}\widetilde{\boldsymbol{\Theta}}^T\left(-\omega^2\mathbf{M} + j\omega\mathbf{C} + \mathbf{K} + j\omega\left(\frac{1}{R_l} + j\omega C_p\right)^{-1}\widetilde{\boldsymbol{\Theta}}\widetilde{\boldsymbol{\Theta}}^T\right)^{-1}\mathbf{r} \tag{36}$$

which from now on is defined as $H(\omega)$. Note that this relationship is independent of the excitation amplitude since it represents the linear relation between the excitation and the response. In other words, it is a valid approach for any excitation amplitude as long as the device behaves linearly, which is the underlying assumption in the present work.

3. Validation of the PEH model

First, the implementation is validated by comparing our results with the results available in the literature. Two geometrical configurations are considered. First configuration is a cantilevered plate of a rectangular shape. Rectangular cantilevered PEHs have been extensively studied in the literature, adopting various theories and approaches. In Ref. [7,8] modal expansions assuming Bernoulli beam theory were developed. Erturk and Iman in Ref. [8] derived an analytical beam model and compared their solutions with the experimental results. Kirchhoff-Love plate theory paired with FEM was used in Ref. [9]. FRF results obtained in Refs. [9] for narrow plates show an excellent agreement with the analytical solutions, obtained from the beam theory and with the experimental data [8]. Since our studies are based on the same Kirchhoff-Love bimorph plate model as in Refs. [9], and the only difference in the results is due to the numerical method (FEM vs. IGA), we therefore focus on the comparison of our results with the data from Ref. [9]. In order to perform comparison not only in terms of accuracy, but also in terms of the computational time, we replicated FEM results from Ref. [9] with our own FEM code.

Second configuration is a circular plate with simply supported or clamped boundary conditions. This problem was studied in Ref. [38] (analytical solution for a Kirchhoff-Love plate), in Ref. [9] (FEM for a Kirchhoff-Love plate), in Ref. [39] (analytical solution and 3D-FEM for a Mindlin plate), and in Ref. [40] (analytical solution for a Reddy plate). Our results are compared with all aforementioned solutions in terms of natural frequencies and vibration modes. It is worth mentioning that all these models (in contrast to the present model) are based on a varying electric field along the PEH.

3.1. Rectangular PEHs

In this section, we consider a PEH, composed of two PZT-5 layers joined to a brass substructure, with a mass at the tip. General characteristics and electro-mechanical properties are given in Tables 1 and 2, respectively. A serial connection is assumed.

In Fig. 2, the voltage FRFs are shown for R_l =1, 6.7, 11.8, 22, 33, 47, 100 and 470 $k\Omega$. The yellow solid lines correspond to the FEM while the blue dotted lines correspond to the IGA approach. It can be seen, that IGA results are in excellent agreement with the FEM data, which in its turn coincides with the results from Ref. [9]. Note that FRFs obtained by the FEM were validated by the experimental results in Refs. [9], therefore, the IGA model is indirectly validated by experiments. The FEM approach

Table 1
General characteristics of the PEH employed to perform the validation. The characteristic presented were extracted from Ref. [8,9].

Length	50.8	[mm]
Width	31.8	[mm]
Thickness of the substructure	0.14	[mm]
Thickness of the PZT layers	0.26	[mm]
Young's modulus of the substructure	105	[GPa]
Mass density of the substructure	9000	[kg/m^3]
Tip mass	0.012	[kg]
Proportional constant (α_o)	14.65	[rad/s]
Proportional constant (β_o)	10^{-5}	[rad/s]
Poisson ratio (ν)	0.3	

Table 2
Electro-mechanical properties of the piezoelectric layers employed in the validation. Corresponding to a PZT-5 piezoelectric ceramic with properties obtained from Ref. [8,9,35].

$\overline{c}_{11}$	69.5	[GPa]
$\overline{c}_{12}$	24.3	[GPa]
$\overline{c}_{66}$	22.6	[GPa]
$\overline{e}_{31}$	−16.0	[C/m^2]
$\overline{\varepsilon}_{33}$	9.57	[nF/m]

employs triangular elements with 3 degrees of freedom per node (deflection in z-direction together with rotations in $x-z$ and $y-z$ planes according to the reference system introduced in Fig. 1), plus one additional degree of freedom corresponding to the element voltage. The FEM results shown in Fig. 2 correspond to a total number of degree of freedoms equal to 6075. On the other hand, the IGA employs 1444 degrees of freedom using NURBS basis functions of $p = q = 6$.

The FEM and IGA models are further compared in terms of accuracy per degree of freedom. The fundamental frequency ω_o, calculated either by FEM or IGA, is compared with the reference solution ω_o^*, obtained using the FEM with a fine mesh (6075 degrees of freedom). A parameter ε is introduced as

$$\varepsilon = \frac{|\omega_o - \omega_o^*|}{\omega_o^*} \tag{37}$$

Convergence plots for ε as a function of the number of degrees of freedom (DOF) are shown in Fig. 3 for various degrees of polynomials p =2, 3, 4, 5, 6 (note that $p = q$ in the IGA model). The results show that both the FEM and the IGA solutions converge with a constant rate to the reference value ω_o^*. The IGA and the FEM of the same degree p =3 yields very similar results with the FEM being slightly more accurate than the IGA for low number of DOFs. The IGA convergence rate and the accuracy increases with p for $2 \leq p \leq 5$, but if p is increased beyond 5, no improvement in the accuracy or the convergence rate is noted in the given DOF range.

The last comparison between the IGA and FEM models is done in terms of computational time. Fig. 4 presents plots of ε with respect to the total time taken by the FRF calculations (in all cases, the simulations were carried out for 1000 excitation frequencies around the first natural frequency). Note, that curves shown in Fig. 4 correspond to the data in Fig. 3, and the values of the mesh refinement level for each data point are also shown (h =1, 2, 3, 4, 5).

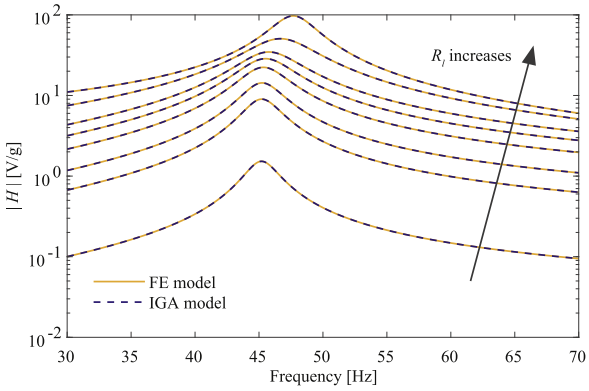

Fig. 2. FRF for the PEH for electrical resistance R_l equal to 1, 6.7, 11.8, 22, 33, 47, 100 and 470 $k\Omega$, comparison between IGA and FEM models.

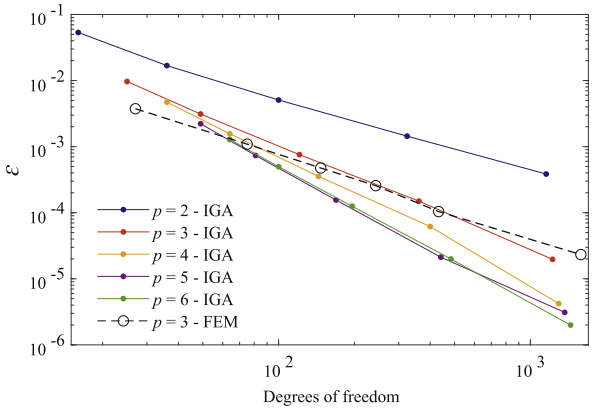

Fig. 3. Comparison of FEM and IGA with NURBS of different degrees in terms of ε vs. the number of degrees of freedom.

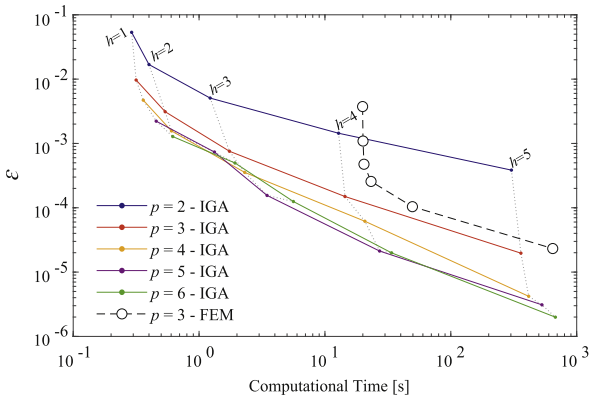

Fig. 4. Comparison of FEM and IGA with NURBS of different degrees in terms of ε vs. the computational time.

From Figs. 3 and 4, it can be concluded that the IGA model for $p, q \geq 3$ offers more accurate results in less time compared with the FEM model. Note that this feature is highly relevant to the computational cost of the shape optimization performed in section 5, as well as to other applications, which require high number of simulations (e.g. uncertainties quantification [29,41]).

For the sake of simplicity, all results presented in this work correspond to the short circuit condition, however, any other configuration follows a similar trend.

3.2. Circular PEHs

In order to evaluate performance of IGA for models with more complex geometries, we analyze a PEH of a circular shape. As shown in Fig. 5, the PEH is composed again of a central substructural layer and two piezoelectric layers bounded to its upper and lower faces. The radius of the plate is $r_o = 600$ mm, thickness of the substructural layer $h_s = 20$mm. Two layers of piezoelectric material PZT-4 have thickness $h_s = 2$mm each, and the electrodes of each piezoelectric layer are assumed to be short-circuited. The corresponding electro-mechanical properties are presented in Table 3. Two boundary conditions are studied: clamped and simply supported boundary. Circular geometry is parameterized with one Coons patch, which is subsequently $p-$ and $h-$ refined. Results are shown for a NURBS basis with $p = q = 6$ and a total of 1444° of freedom.

The first four natural frequencies of a circular PEH with clamped boundary are calculated. Their respective values and modes are presented in Table 4 and Fig. 6. In addition, the solutions reported in the literature are also given in Table 4. Specifically, the proposed IGA is compared with formulations based on: (a) analytic solution employing Kirchhoff-Love plate theory (Kirchhoff-Analytic) [38], (b) FEM solution employing Kirchhoff-Love plate theory (Kirchhoff-FEM) [38], (c) analytic solution employing Mindlin plate theory (Mindlin-Analytic) [39], (d) Fully three-dimensional FEM (3D-FEM) [39], and (e) analytic solution employing Reddy plate theory (Reddy-Analytic) [40]. The relative difference between the IGA result and the corresponding reference solutions is shown in parenthesis. In general, it is observed that natural frequencies obtained with the proposed IGA model agree well with the values reported in the literature, identifying differences within 1.1%. Note, that difference in the results is due to the difference in the plate model and the approximation error in the numerical method.

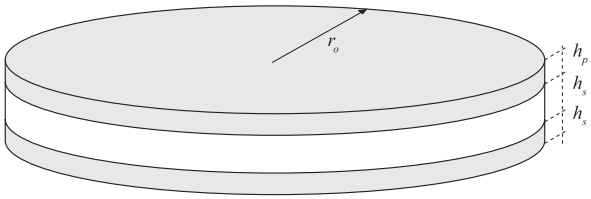

Fig. 5. Scheme of a circular bimorph PEH.

Table 3
Electro-mechanical properties of the circular PEHs.

Substructure		
ρ_s	7800	[kg/m^3]
Y_s	200	[GPa]
Piezoelectric layer PZT-4		
$\overline{c}_{11}$	85.6	[GPa]
$\overline{c}_{22}$	85.6	[GPa]
$\overline{c}_{12}$	24.6	[GPa]
$\overline{c}_{66}$	30.5	[GPa]
$\overline{e}_{31}$	−13.0	[C/m^2]
$\overline{e}_{32}$	−13.0	[C/m^2]
$\overline{\varepsilon}_{33}$	17.6	[nF/m]

Similarly to the previous case, Table 5 shows the first four natural frequencies calculated for a PEH with simply supported boundary, while their respective modes are shown in Fig. 7. The values reported in the literature together the relative difference with respect to the IGA model are also presented. Again, a good agreement between results can be seen, with differences within 0.77%.

3.3. Experimental validation

Additionally to the numerical validation presented in previous sections, the FRF obtained using the IGA model is further compared with the experimental data. Here, two PEHs with different geometries are tested following the procedure introduced in Ref. [31]. The first configuration corresponds to a rectangular PEH with nominal characteristics presented in Tables 1 and 2 employing a shunt resistance equal to 1 $k\Omega$. The second configuration corresponds to a triangular device with the same characteristics as the previous case, except that the width at the base is 31.8 mm and 0 mm at the free end. As can be seen in Fig. 8, the experimental FRFs are in a good agreement with the IGA results indicating the suitability of the proposed model to predict

Table 4
Comparison of natural frequencies [rad/s] of a circular PEH configuration for clamped boundary condition with reference solutions from the literature. Relative difference between the IGA solution and the corresponding reference solution is given in parenthesis.

Method	1st mode		2nd mode		3rd mode		4th mode	
IGA in this work	901.99		1875.94		3074.87		3505.42	
Kirchhoff-Analytic [38]	902.48	(0.1%)	1878.17	(0.1%)	3081.08	(0.2%)	3513.43	(0.2%)
Kirchhoff-FEM [38]	900.15	(0.2%)	1866.90	(0.5%)	3050.90	(0.8%)	3475.20	(0.9%)
Mindlin-Analytic [39]	899.10	(0.3%)	1864.10	(0.6%)	3044.70	(1.0%)	3468.30	(1.1%)
3D-FEM [39]	900.10	(0.2%)	1862.70	(0.7%)	3050.90	(0.8%)	3475.20	(0.9%)
Reddy-Analytic [40]	899.22	(0.3%)	1864.73	(0.6%)	3046.37	(0.9%)	3470.35	(1.0%)

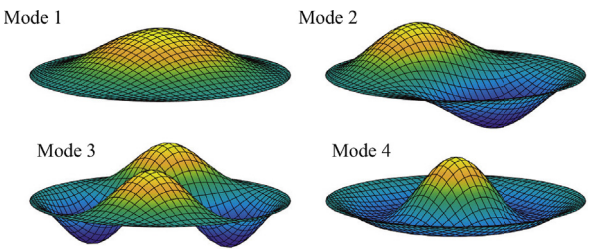

Fig. 6. First four modes of the circular PEH with clamped boundary.

Table 5
Comparison of natural frequencies [rad/s] of a circular PEH configuration for simply supported boundary condition with reference solutions from the literature. Relative difference between the IGA solution and the corresponding reference solution is given in parenthesis.

Method	1st mode		2nd mode		3rd mode		4th mode	
IGA in this work	435.43		1226.20		2258.32		2619.76	
Kirchhoff-Analytic [38]	435.64	(0.1%)	1227.49	(0.1%)	2262.44	(0.2%)	2625.23	(0.2%)
Mindlin-Analytic [39]	435.10	(0.1%)	1221.40	(0.4%)	2241.10	(0.8%)	2605.50	(0.5%)
3D-FEM [39]	435.20	(0.1%)	1218.50	(0.6%)	2242.40	(0.7%)	2606.50	(0.5%)
Reddy-Analytic [40]	435.15	(0.1%)	1221.63	(0.4%)	2241.80	(0.7%)	2606.27	(0.5%)

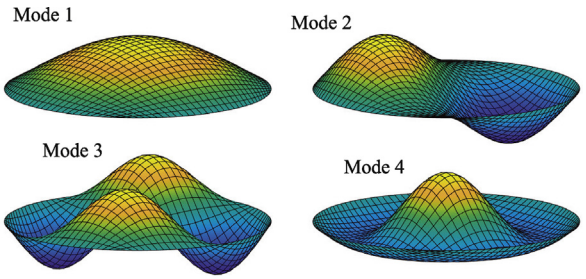

Fig. 7. First four modes of the circular PEH with simply supported boundary.

the dynamic behaviour of PEHs. Here, it is important to mention that the discrepancies between simulations and experimental results could be decreased by adopting a parameter identification technique, for a more detailed information please refers to Ref. [42] where a Bayesian Inference is apply to identify electromechanical properties in PEHs.

4. Parametric study of PEHs of different shapes

The developed IGA model is used to conduct a parametric study of three families of boundary shapes. The idea of this section is to highlight the capability of the developed approach to analyze complex geometries and to select the best candidate in terms of output voltage. The three parametric families of boundary shapes are shown in Fig. 9. The study is conducted in terms of the first natural frequency ω_o, the peak of FRF H_o and its value per unit of surface area (H_o/S).

The simplest configuration is a rectangle (identified as Type-A in Fig. 9), entirely defined by two parameters: length L and width W (or length L and the aspect ratio $R = W/L$). The second configuration is represented by a curved boundary (Type-B in Fig. 9). Here, the geometry is described by three parameters: length L, width W and parameter δ, which represents deviation of the shape from a straight line. The boundary curve is defined by NURBS of order $p = q = 3$, such that the curve passes through points $(1/4L, W - \delta)$ and $(3/4L, W + \delta)$. The geometry, shown in Fig. 9 corresponds to positive δ, but in the parametric study $\delta \in (-W/2, W/2)$ was considered. Note, that the two boundaries along the length of the harvester are symmetric with respect to the middle line. It is convenient to introduce dimensionless parameters $R = W/L$ and $r = \delta/W$ instead of W and δ. Then, by varying the length L, the PEH can be scaled to a particular size, while the dimensionless ratios R and r define a respective shape. Therefore, the parametric family includes configurations with the same shape (i.e., the same r and R) but different sizes (i.e., different L). Finally, the third parametric family corresponds to a trapezoidal geometry (Type-C in Fig. 9), defined by three parameters: L, $R = W/L$ and angle α. Note, that α is allowed to take both, positive and negative values. Left and right boundaries

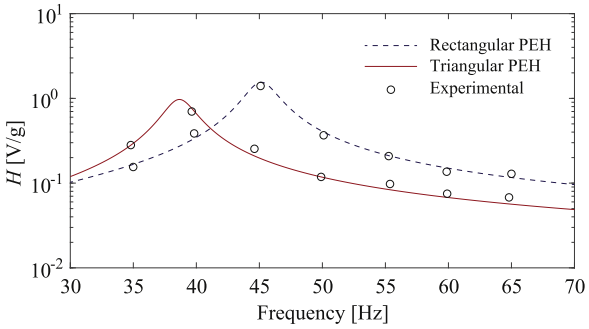

Fig. 8. FRF for rectangular and triangular PEHs. Comparison of the IGA results with the experimental data. In both cases, the proportional damping coefficients employed corresponds to $\alpha_o = 14.65$ rad/s and $\beta_o = 10^{-5}$ rad/s.

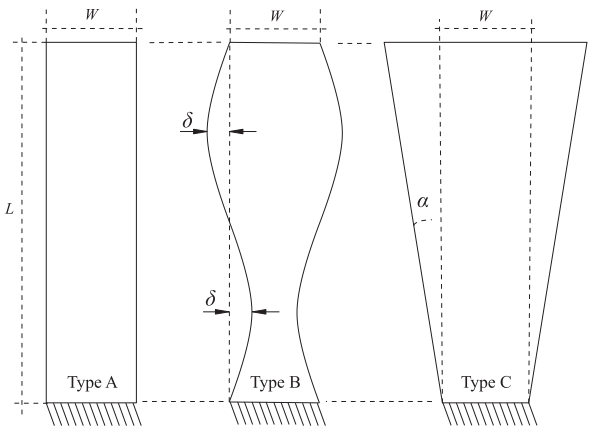

Fig. 9. Different types of PEHs: rectangular (Type-A), curved (Type-B), and trapezoidal (Type-C) plates.

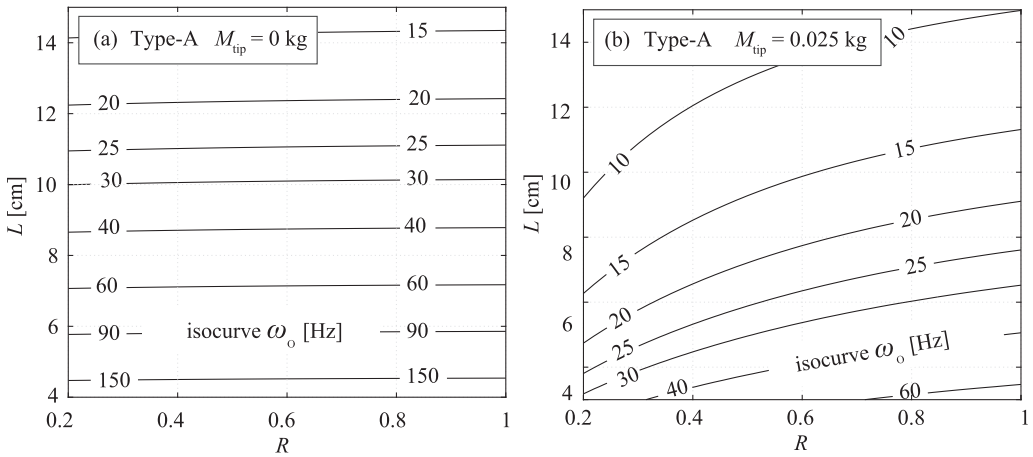

Fig. 10. Isocurves for fundamental frequency ω_o for Type-A PEHs. (a) Maps without tip mass. (b) Maps with a tip mass of 0.025 kg.

are symmetric with respect to the middle line. Note that the mentioned geometries correspond to configurations previously explored in the literature, see for instance Refs. [10–14,17], being the most common configurations adopted in piezoelectric energy harvesting. The material properties employed here corresponds to the case studied earlier in Section 3.1 (reference values are reported in Tables 1 and 2). Here, it is important to mention that a uniform thickness is assumed along the device, while the proportional damping constants $\alpha_o = 14.65$ rad/s and $\beta_o = 10^{-5}$ rad/s are considered invariant. The later assumption is important since it implies variations in the damping ratio with respect to the device stiffness and mass. As a consequence, any variation in the geometry or in the tip mass will changes the damping ratio. This assumption is supported in the analysis conducted by Junior et al., in 2009 [9], which corresponds to the reference case to perform the parametric analysis presented here.

4.1. Effect on the fundamental frequency

The effect of the shape, size and tip mass on the fundamental frequency of the PEH is studied first. Fig. 10 shows the isocurves for ω_o in the plane (R, L) for rectangular PEHs (Type-A) when no mass is added at the tip (Fig. 10(a)) and when a tip mass $M_{tip} = 0.025$ kg is used (Fig. 10(b)). As expected, in both cases, the fundamental frequency decreases with increasing length L. However, in the case when M_{tip} =0, the fundamental frequency is almost independent of R.

A similar analysis is shown in Fig. 11 for the Type-B device. In this case, the figure shows the isocurves for ω_o in plane (R, r) for two different length: L =10 cm (Fig. 11(a)) and L =5 cm (Fig. 11(b)), both considering no mass at the tip. The third plot is also presented (Fig. 11(c)) to study the impact of the tip mass over the isocurves for ω_o. Note that the main difference between the geometries of Fig. 11(a) and (b) is the size of the device but not the shape, while the difference between Fig. 11(b) and (c) is only the presence of the tip mass, i.e. the PEHs presented in each plot have the same shape but different sizes or tip masses. In the absence of tip mass, the fundamental frequency is again almost independent of R, being L and r the two parameters with greater

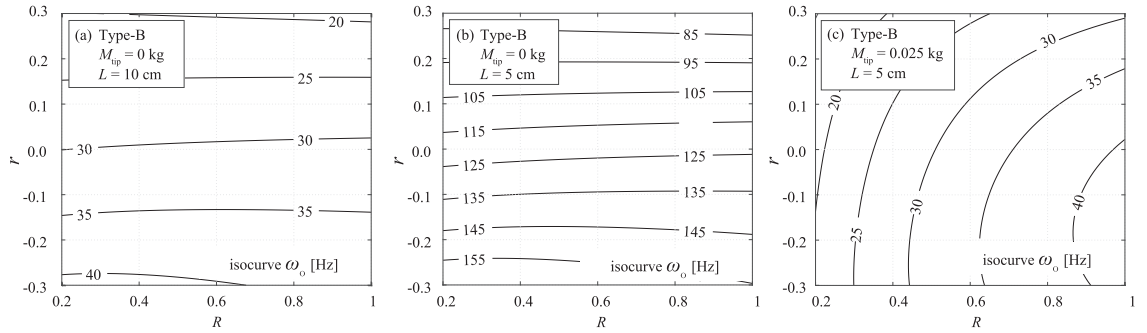

Fig. 11. Isocurves for fundamental frequency ω_o for Type-B PEHs. (a) Map without a tip mass for $L = 10$ cm. (b) Map without a tip mass for $L = 5$ cm. (c) Map for a tip mass of 0.025 kg and $L = 5$ cm.

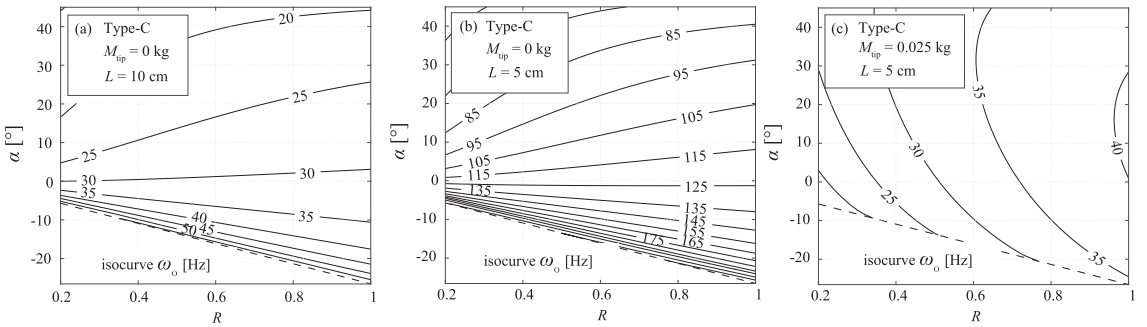

Fig. 12. Isocurves for fundamental frequency ω_o for Type-C PEHs. (a) Map without a tip mass for $L = 10$ cm. (b) Map without a tip mass for $L = 5$ cm. (c) Map for a tip mass of 0.025 kg and $L = 5$ cm.

influence on ω_o. In general, if L and r are increased, then ω_o is decreased. However, the tip mass has an important impact on ω_o not only changing its value but also introducing a strong dependence on R.

The isocurves for Type-C devices are studied following an analysis similar to the one employed for Type-B devices. The results are presented in Fig. 12, where the isocurves for ω_o are presented in plane (R, α). The main observation here has to do with the fact that the three geometrical parameters (R, L, α) present an important influence on ω_o. Moreover, this observation is independent of the tip mass. Only for small angles ($\pm 5°$) and absence of tip mass, the devices exhibit a small dependence on R (Fig. 12(a) and (b)), which is expected since it corresponds to shapes close to Type-A devices.

Although the three devices studied are different in shapes and sizes, there still some general remarks that are considered important to highlight: (1) In the absence of tip mass, R is the less sensitive parameter that affects ω_o, (2) the use of a tip mass increases the sensitivity of all the geometrical parameters over ω_o, (3) it is possible to enforce a specific ω_o with any type of device studied with or without tip mass, and (4) if a specific ω_o is desired, the addition of a tip mass leads to smaller devices. However, by studying only ω_o, it is not sufficient to identify which type of device outperforms the others since no direct information about the output voltage is offered. In order to address this issue, the following section moves the discussion to the comparison between devices in terms of the output voltage.

4.2. Effect on the output voltage

The metric employed to compare the output voltage of the three types of devices corresponds to the maximum value of the FRF H_o, i.e., the amplitude of the FRF at ω_o. In particular, two configurations of each type of device are presented, incorporating configurations with and without tip mass. The results are presented in Fig. 13 in terms of isocurves for H_o. The first (Fig. 13(a) and (b)), second (Fig. 13(c) and (d)) and third columns (Fig. 13(e) and (f)) of figures correspond to Type-A, Type-B and Type-C configurations, respectively. On the other hand, the first (Fig. 13(a), (c) and 12(e)) and second rows (Fig. 13(b), (d) and 12(f)) of figures correspond to devices without and with tip mass, respectively. Note that for the case in which the Type-B and Type-C present a tip mass (Fig. 13(d) and (f)), the length of the device is fixed to $L = 5$cm. The motivation behind this selection is to enforce fundamental frequencies similar to the case in which no tip mass is considered (where $L = 10$cm). In this sense, and to have a common reference point, it is decided to include also the isocurves for $\omega_o = 30$ Hz (shown in red dotted lines). The first interesting result deals with the fact that isocurves for H_o are higher in absence of tip mass for any type of geometry. In particular, the higher H_o for Type-A are found for large R and L; while large R and lower r, and large R and α, lead to higher H_o

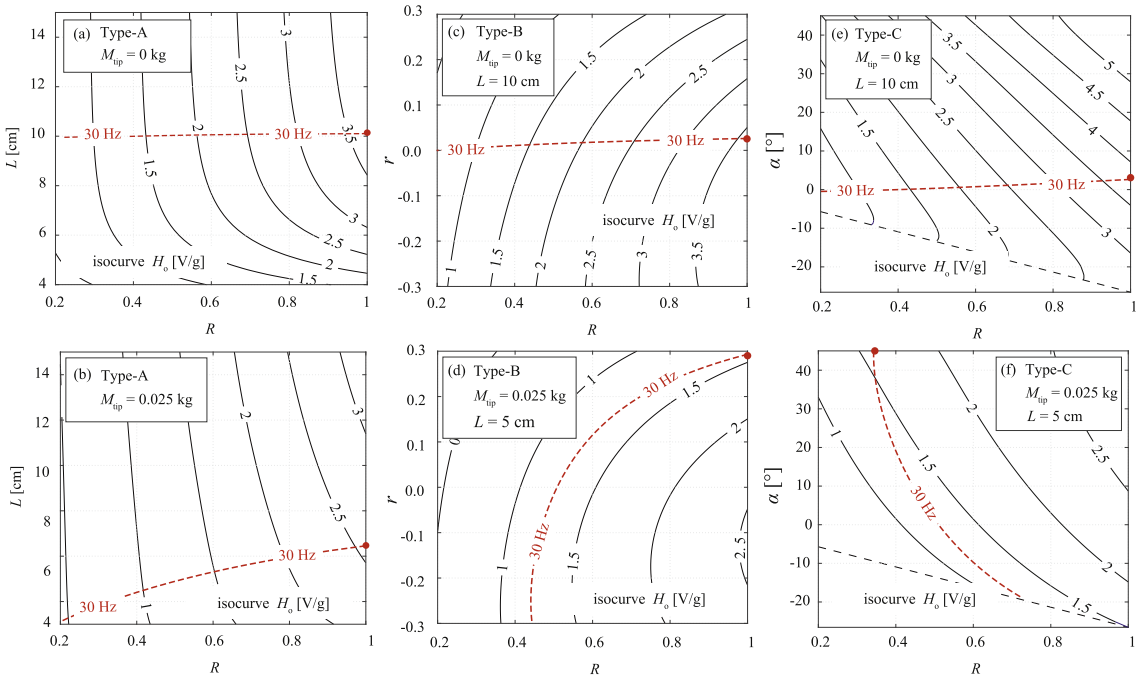

Fig. 13. Isocurves for maximum amplitude of FRF H_o. (a) Map for Type-A without tip mass. (b) Map for Type-A with a tip mass of 0.025 kg. (c) Map for Type-B without tip mass and L = 10 cm. (d) Map for Type-B with a tip mass of 0.025 kg and L = 5 cm. (e) Map for Type-C without tip mass and L = 10 cm. (f) Map for Type-C with a tip mass of 0.025 kg and L = 5 cm. The red dotted lines correspond to isocurves for ω_o = 30 Hz, while the red circle corresponds to the optimal configuration for ω_o = 30 Hz. (For interpretation of the references to color in this figure legend, the reader is referred to the Web version of this article.)

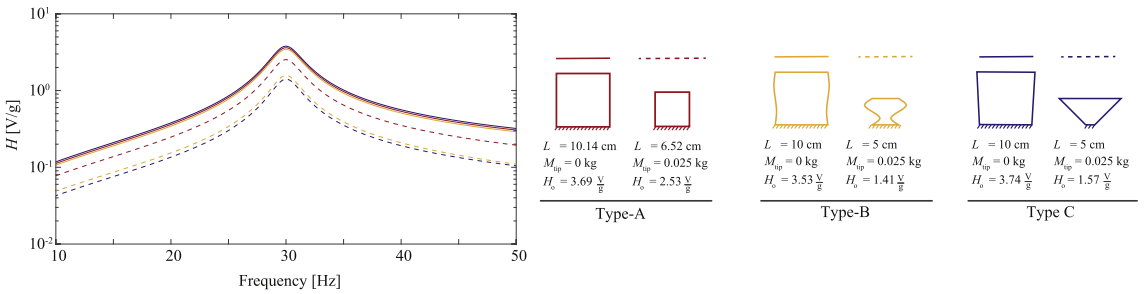

Fig. 14. FRF for optimal geometries associated to Type-A (red), Type-B (yellow) and Type-C (blue), with ω_o = 30 [Hz]. The solid lines are the PEHs without a tip mass and the dotted lines are PEHs with tip mass M_{tip} = 0.025 kg. (For interpretation of the references to color in this figure legend, the reader is referred to the Web version of this article.)

for Type-B and Type-C, respectively. These results are particularly useful when the PEH is excited with a broadband frequency since it enforces a resonance operation.

On the other hand, excitations with a narrow frequency band oblige to select a PEH such that the fundamental frequency matches the excitation. In order to exemplify this condition, it is decided to study the best candidate of each configuration for a fixed fundamental frequency, in this case ω_o = 30 Hz. The best candidate here is defined as the configuration that gives the higher H_o constrained to a ω_o = 30 Hz. This candidate is identified in each plot as a red solid circle. The six candidates (best geometry of each type considering and non considering the tip mass) are now compared in Fig. 14, where it is possible to observe the behaviour of their respective FRF. The information in the figure is organized as follows: colors red, yellow and blue indicate Type-A, Type-B and Type-C, respectively. Additionally, solid lines correspond to configurations without tip mass while dotted lines correspond to configuration with a tip mass. The figure also shows the shape of each candidate keeping the same scale to have a reference point. For the case studied, the optimal configuration corresponds to Type-C device with R =1 and α = 4°, giving a H_o =3.74 V/g. However, Type-A and Type-B configuration are not as different since they arrived to similar geometries reaching values up to H_o =3.69 V/g and H_o =3.53 V/g, respectively. Also, these small differences are also observed in the FRFs presented, where the solid lines are close to each other. Even more, it can be concluded from the significant difference between the solid and dotted lines, that the configurations without tip mass outperform the configurations with a tip mass.

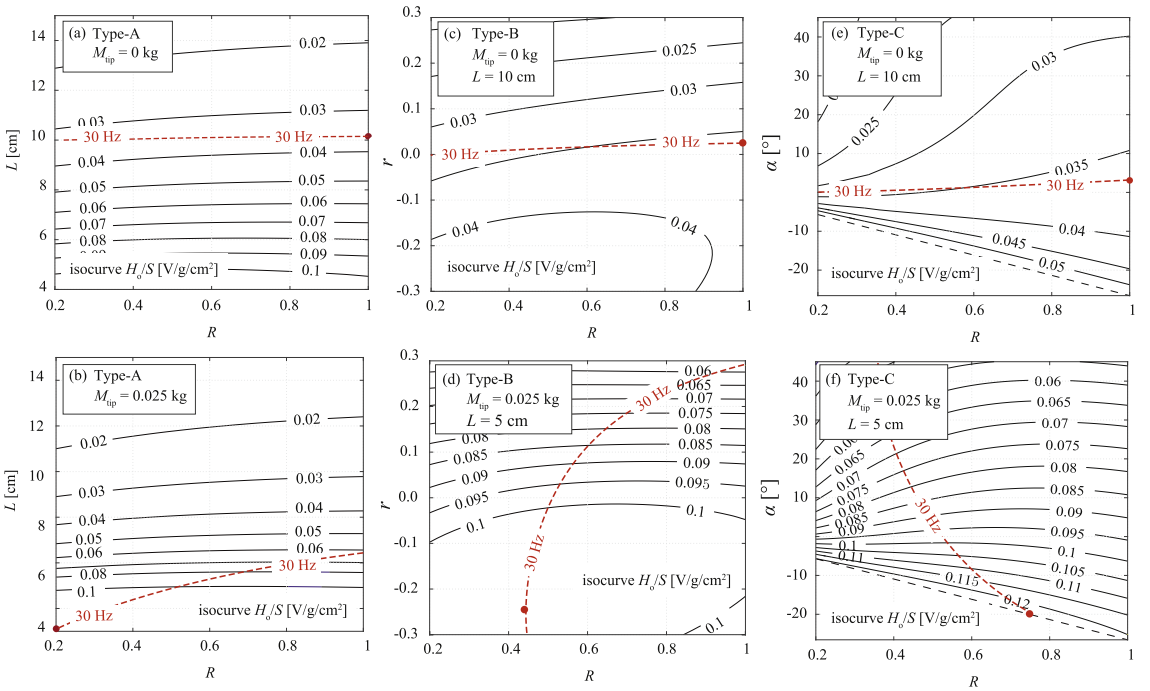

Fig. 15. Isocurves for maximum amplitude of FRF per unit of area H_o/S. (a) Map for Type-A without tip mass. (b) Map for Type-A with a tip mass of 0.025 kg. (c) Map for Type-B without tip mass and L = 10 cm. (d) Map for Type-B with a tip mass of 0.025 kg and L = 5 cm. (e) Map for Type-C without tip mass and L = 10 cm. (f) Map for Type-C with a tip mass of 0.025 kg and L = 5 cm. The red dotted lines correspond to isocurves for ω_o = 30 Hz, while the red circle corresponds to the optimal configuration for ω_o = 30 Hz. (For interpretation of the references to color in this figure legend, the reader is referred to the Web version of this article.)

Although the optimal configuration for ω_o =30 Hz corresponds to almost a square device, it is not necessary the best configuration in terms of voltage per unit of superficial area (or device volume). The studies of the output voltage or power per unit of volume have been conducted before, see for instance Ref. [10,13,14], where it is concluded that the devices with tip masses increase the output energy density (voltage or power divided by the device volume). In order to highlight this fact, the following section presents an analysis of the output voltage per unit of superficial area H_o/S.

4.3. Effect on the voltage per unit of area

In this instance, the results are presented in Fig. 15 to show the behaviour of the isocurves for H_o/S. The configurations employed here correspond to the same configurations used in Fig. 13. Here, it is evident that the devices with a tip mass outperform the devices without a tip mass. In particular, Type-C geometries with large R and lower α arrived to the higher values of H_o/S, which corresponds to geometries with trapezoidal characteristics where the fixed base is wider than the free end of the device. This result is in agreement with observations previously identified in the literature, for example in Ref. [10,13,14]. Another important observation deals with fact, that the impact of R on H_o/S is less sensitive than the impact on H_o. In other words, the large R implies large H_o but not necessary large H_o/S. Even more, the zone for the higher H_o (Fig. 13) and the zone for higher H_o/S (Fig. 15) are not the same, indicating that it is not possible to simultaneously achieve the maximum H_o and H_o/S. Again, this analysis is done assuming that the device could be excited at its natural frequency (i.e., broadband excitation frequency).

Similar to the case presented in Fig. 13, a reference line for ω_o = 30 Hz is included in red dotted lines to exemplify the effect of narrow-band excitations. The higher value of H_o/S for the constrained frequency (ω_o =30 Hz) is identified as a red circle. Here, the optimal geometrical parameters are selected to be compared in terms of their FRF. These results are shown in Fig. 16 following the same approach of Fig. 14. Results indicate that the best configuration corresponds to the Type-C device with R = 0.73 and α =−20° giving and output voltage of H_o/S = 0.124 V/g/cm^2. When Figs. 14 and 16 are compared, some interesting results are observed. First, in the absence of tip mass, the optimal geometry obtained for H_o and H_o/S is almost the same (essentially a square plate of L =10 cm). However, when the tip mass is allocated, the competing objectives between H_o and H_o/S are observed again.

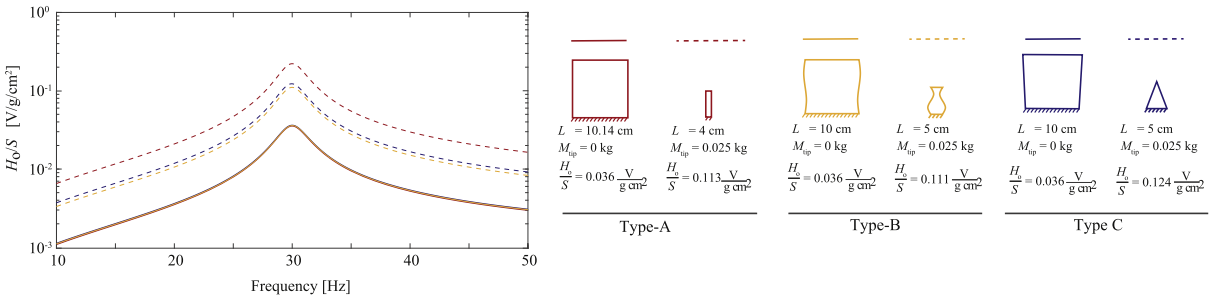

Fig. 16. FRF for optimal geometries associated to Type-A (red), Type-B (yellow) and Type-C (blue), with $\omega_o = 30$ Hz. The solid lines are the PEHs without a tip mass and the dotted lines are PEHs with tip mass $M_{tip} = 0.025$ kg. (For interpretation of the references to color in this figure legend, the reader is referred to the Web version of this article.)

5. Shape optimization of PEHs

The parametric study presented in section 4 reveals the importance to adequately select the shape of the PEH and opens the question about the use of the IGA model as a tool to perform shape optimization. Based on the results already discussed, it is possible to claim that the IGA model is a suitable choice for shape optimization due to mainly its capability to generate an accurately representation of different shapes through NURBS, relatively low computational burden, and important level of precision. In this section, a procedure is proposed to efficiently tackle the selection of PEH geometries such that a specific natural frequency is enforced while the peak output power, voltage or current is maximized. One of the major concerns here is related to non-convex nature of the problem, i.e., PEHs with different shapes could present the same fundamental frequency. To overcome this problem, it is decided to perform shape optimization by adopting a blind search approach over an extensive database generated employing a surrogate metamodel previously trained using the IGA model. Details of this optimization scheme are offered in the following paragraphs.

5.1. Optimization based design

The optimization problem could be presented in the following form

$$\mathbf{x}^* = \underset{\mathbf{x}\in\mathbf{X}}{arg\,max}\ |T(\omega,\mathbf{x})| \quad \text{such that } \omega_{\text{inf}} \le \omega \le \omega_{\text{sup}} \tag{38}$$

where the objective function $T(\omega,\mathbf{x})$ represents some relevant characteristic of the FRF for a given excitation frequency ω and a specific set of control points $\mathbf{x}$. The optimization is established to obtain the set of control points (which fully describe the boundary shape of a device) to maximize $T(\omega,\mathbf{x})$ in a particular range of frequencies $[\omega_{\text{inf}},\omega_{\text{sup}}]$. In the context of the discussion offered in Section 4 about the selection of the PEH in terms of the power density (greater electrical power in lower volume), the objective function could be modified to support a multiobjective optimization of $H_o(\omega,\mathbf{x})/S(\mathbf{x})$ and $H_o(\omega,\mathbf{x})$. This multi-objective formulation leads ultimately to a set of points (also known as dominant designs) that lie on the boundary of the feasible objective space and form a manifold: the Pareto front. A point belongs to the Pareto front and it is called Pareto optimal point if there is no other point that improves one objective without detriment to any other.

The optimization seeks to identify geometries (defined by the control points $\mathbf{x}$) that present a fundamental frequency lying in the interest range of frequencies and that give the FRF with the higher peak or the higher peak per superficial area. Here, it is important to highlight, that the search space $\mathbf{X}$ is limited by the designer criteria over a fixed number of control points. An increment in the number of control points also increases the universe of possible geometries that could be generated. This presents an important challenge from the computational point of view since the optimization could lead to multi-optimal designs, i.e. the objective function leads to a non-convex problem. To carry out this task, an efficient optimization scheme based on a Kriging metamodeling is proposed and presented in the following section.

5.2. Kriging-aided optimization

Kriging provides a simplified relationship between the input and output of a process utilizing existing information (database) for them. Let $\boldsymbol{\theta}\in R^{n_\theta}$ and $\mathbf{g}\in R^{n_g}$ denote the input and output, respectively, and $\{\boldsymbol{\theta}^k-\mathbf{g}^k : k=1,\dots,n_{\text{sup}}\}$ the available database (training set) of n_{sup} number of $\boldsymbol{\theta}-\mathbf{g}$ pairs of data (also known as support points). The fundamental building blocks of Kriging are the n_p dimensional quadratic basis vector $\mathbf{f}(\boldsymbol{\theta})$

$$\mathbf{f}(\boldsymbol{\theta}) = \left[1\ \ \theta_1\ \ \dots\ \ \theta_{n_\theta}\ \ \theta_1^2\ \ \theta_1\ \ \theta_2\ \ \dots\ \ \theta_{n_\theta}^2\right]\ ;\ n_p = (n_\theta+1)(n_\theta+2)/2 \tag{39}$$

and the generalized exponential correlation function $R(\boldsymbol{\theta}^m, \boldsymbol{\theta}^n)$

$$R(\boldsymbol{\theta}^m, \boldsymbol{\theta}^n) = \prod_{i=1}^{n_\theta} \exp[-s_i|\theta_i^j - \theta_i^k|^{s_{n_\theta+1}}] \; ; \; \mathbf{s} = \left[s_1 \dots s_{n_\theta+1}\right] \tag{40}$$

For the set of n_{sup} of inputs and outputs (database); the input, output, and basis matrices are defined as

$$\begin{aligned} \boldsymbol{\Phi}_\mathbf{o} &= \left[\boldsymbol{\theta}^1 \dots \boldsymbol{\theta}^{n_{\text{sup}}}\right]^T \\ \mathbf{G}_\mathbf{o} &= \left[\mathbf{g}^1 \dots \mathbf{g}^{n_{\text{sup}}}\right]^T \\ \mathbf{F}_\mathbf{o} &= \left[\mathbf{f}(\boldsymbol{\theta}^1) \dots \mathbf{f}(\boldsymbol{\theta}^{n_{\text{sup}}})\right]^T \end{aligned} \tag{41}$$

Additionally, a correlation matrix $\mathbf{R}_\mathbf{o}$ is defined such that each nm-element is obtained evaluating the correlation function $R(\boldsymbol{\theta}^m, \boldsymbol{\theta}^n)$. Ultimately, the Kriging approximation of the input output relationship is given by

$$\mathbf{g}_{\mathbf{kri}}(\boldsymbol{\theta}) = \mathbf{f}(\boldsymbol{\theta})^T \boldsymbol{\alpha}_\mathbf{o} + \mathbf{r}(\boldsymbol{\theta})^T \boldsymbol{\beta}_\mathbf{o} \tag{42}$$

where $\mathbf{g}_{\mathbf{kri}}(\boldsymbol{\theta})$ corresponds to the Kriging output estimation for a given new input $\boldsymbol{\theta}$, while $\boldsymbol{\alpha}_\mathbf{o}$, $\boldsymbol{\beta}_\mathbf{o}$, and $\mathbf{r}(\boldsymbol{\theta})$ are defined as:

$$\boldsymbol{\alpha}_\mathbf{o} = (\mathbf{F}_\mathbf{o}^T \mathbf{R}_\mathbf{o}^{-1} \mathbf{F}_\mathbf{o})^{-1} \mathbf{F}_\mathbf{o}^T \mathbf{R}_\mathbf{o}^{-1} \mathbf{G}_\mathbf{o} \tag{43}$$

$$\boldsymbol{\beta}_\mathbf{o} = \mathbf{R}_\mathbf{o}^{-1} (\mathbf{G}_\mathbf{o} - \mathbf{F}_\mathbf{o} \boldsymbol{\alpha}_\mathbf{o}) \tag{44}$$

$$\mathbf{r}(\boldsymbol{\theta}) = \left[R(\boldsymbol{\theta}, \boldsymbol{\theta}^1) \dots R(\boldsymbol{\theta}, \boldsymbol{\theta}^{n_{\text{sup}}})\right]^T \tag{45}$$

The Kriging tuning involves an optimization process where the parameter $\mathbf{s}$ is identified such that eq. (39) could be used to interpolate new points in the database. Once the Kriging metamodel is tunned, it accuracy could be evaluated adopting a leave-one out cross validation. Details on this Kriging tuning and validation could be found in Ref. [43,44].

Ultimately, the Kriging is used to surrogate a high fidelity model, where the later is used to fill the database needed for the Kriging tuning. The derivation of the database is formally known as DoE (Design of Experiments) and common approach is to use a space filling algorithm for it (such as Latin Hypercube Sampling [45]) within the range $\boldsymbol{\Theta}$ of possible values for $\boldsymbol{\theta}$.

For the particular application in PEHs, it is decided to surrogate the relation between the position of the control points $\mathbf{x}$ and variables associated to: superficial area of the device S, first natural frequency ω_o, and the amplitude of the FRF at ω_o (identified here as H_o); obtaining the following relation based on the surrogated model

$$\left[S \;\; \omega_o \;\; H_o\right] = \mathbf{g}_{\mathbf{kri}(x)} \tag{46}$$

Once $\mathbf{g}_{\mathbf{kri}(x)}$ is properly tuned, the database could be significantly augmented by the addition of new input-output pairs estimated with the Kriging metamodel. Finally, a blind search approach [46] is employed over the augmented database to extract the control points that corresponds to devices with natural frequencies in the $[\omega_{\text{inf}}, \omega_{\text{sup}}]$ range. After that, a second blind search could be perform to extract the control points with the greater values of H_o or H_o/S. Please refers to Ref. [47,48] where similar optimization approaches have been applied for other kind of problems.

5.3. Illustrative implementation

Different optimization examples are carried on evaluating the effectiveness and performance of the method. These examples describe the optimization of a Bimorph PEH, with the electromechanical properties corresponding to PZT-5 layers and brass substructure presented in Tables 1 and 2 The boundary shape is assumed to be symmetric with respect to the middle line ($y = 0$). The boundary curve is parameterized with NURBS of $p = 3$ and 8 control points. For any length L and width W, the locations of the two end points are fixed at $(0, W/2)$ and $(L, W_L/2)$, and the inner points are distributed evenly between. The shape is controlled by $W \in L \times [0.3, 1]$ and the position in the y-direction of the inner points (Fig. 1), the upper points are moved in the interval $\frac{W}{2} \times [0.02, 3]$ while the position of the lower inner points are definite such that to obtain a symmetric shape respect to the y-axis. Therefore, the geometry is described by eight design parameters: $L \in [2,10]$ cm, W and y-coordinates of the six control points. If the tip mass M_{tip} is included in the optimization, the design space consists of nine variables $\mathbf{x}$. It is assumed, that $M_{tip} \in [0, 0.025]$ kg.

A Kriging metamodel is employed to surrogate the relations between the nine design variables $\mathbf{x}$ and the three outputs $[S \; \omega_o H_o]$ by using 30.000 support points. The accuracy of the metamodels is high, with the correlation coefficient, evaluated using leave-one-out cross validation [49], close to 96% for all approximated response quantities. Two different implementations of the optimization are considered. In the first implementation a specific value of M_{tip} is assumed and optimization is performed over the remaining design variables. This specific choice was made to better examine the impact of M_{tip} on the optimal shape. The respective values used for M_{tip} are 0 and 0.025 kg. In the second implementation all design variables are simultaneously

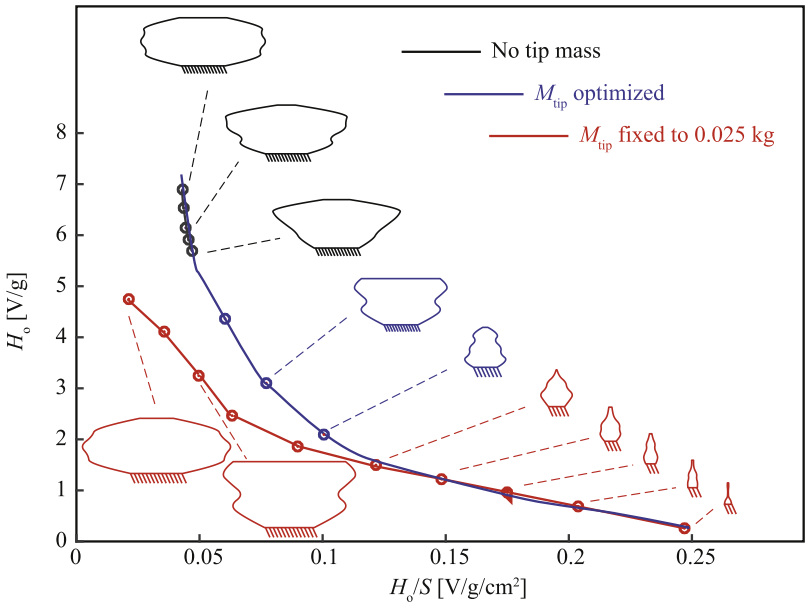

Fig. 17. Pareto front with optimal geometries for the maximization of H_o and H_o/S. Results correspond to devices with $\omega_o = 30$ Hz. Three Pareto fronts are presented: devices without tip mass (black line), devices with tip mass equal to 0.025 kg (red line), and devices where the tip mass is a design variable (blue line). (For interpretation of the references to color in this figure legend, the reader is referred to the Web version of this article.)

optimized. This implementation will be referenced as M_{tip} optimized herein. The Pareto fronts (optimal design points for H_o and H_o/S) are identified using a blind-search: 2 million candidate design configurations for $\mathbf{x}$ are defined within the admissible domain $\mathbf{X}$ using Latin hypercube sampling, performance objectives are estimated (using the developed metamodel) for all of them, and the Pareto front is identified by selecting the dominant designs among these configurations. The large value of candidate design configurations examined for $\mathbf{x}$ ultimately gives features of exhaustive-search to the adopted numerical scheme, facilitating accurate convergence to the actual Pareto front. In order to allow a direct comparison with the results obtained in section 4, it is decided to perform the optimization with a constrain equal to $0.97\omega_o < \omega < 1.03\omega_o$, for $\omega_o = 30$ Hz.

Results of the optimal design are presented in Fig. 17. Here, Fig. 17 shows the Pareto front for the two objectives H_o and H_o/S for: (1) with the tip mass as a design variable (blue solid line), (2) fixed tip mass equal to 0.025 kg (red solid line), and (3) absence of tip mass (black solid line). The competition between the objectives is clear for the three cases studied. The extremes of the Pareto front indicate the optimal designs for H_o and H_o/S. In particular, from the blue line, it is possible to observe that the optimal values of H_o and H_o/S are around 7 V/g and 0.25 V/g/cm^2, respectively, almost double the values obtained in the parametric study performed in section 4. This result highlights the importance of performing the shape optimization in a wide design space. Note also that the extremes of the blue line overlap to the Pareto front obtained by fixing the tip mass to $M_{tip} = 0$ (black line) and $M_{tip} = 0.025$kg (red line), indicating that the current Pareto (blue line) is bounded by these two conditions. Furthermore, the optimal H_o is achieved when no tip mass is used leading to a PEH with a large surface. Contrary, the optimal H_o/S is achieved for the highest tip mass employed ($M_{tip} = 0.025$ kg), corresponding to a small PEH with a narrow tip. Note that the optimal tip mass varies across the front going from zero to the maximum mass accounted. Additionally, it is important to highlight that changes in the tip mass imply changes in the damping ratio since it is considered a proportional damping with constant coefficients $\alpha_o = 14.65$ rad/s and $\beta_o = 10^{-5}$ rad/s. These coefficients are assumed invariant in the optimization to be consistent with the observations made in Ref. [9]. However, it is important to highlight that other works exist, that consider constant damping ratios across the optimization, see for instance Ref. [17]. In this regard, the accounting of damping and its dependency on the device stiffness and mass still needs a more comprehensive study from the experimental perspective. Furthermore, the variation of the optimal geometries from one extreme of the front to the other is also notorious, going from large and wide devices without a tip mass to small and narrow devices with tip masses. Ultimately, the designer could select any configuration from the Pareto point based on the desired balance between the objectives.

6. Conclusions

In this work, an Isogeometric Analysis based framework for Piezoelectric Energy Harvesters is presented. The model is based on the Kirchhoff-love plate theory and the generalized Hamilton's principle for electroelestic bodies. The boundary shape is parameterized by NURBS, enabling complex configurations with a large number of design parameters. The generated voltage is obtained as a response of an excitation acceleration of the base.

The approach is validated in terms of the FRF and natural frequencies against different models available in the literature. The results for the benchmark problems of rectangular and circular shapes are in excellent agreement with the reference solutions. In terms of computational time, IGA of degree $p > 3$ is faster than the FEM analysis with the same accuracy, which is an important advantage in the applications which require generating a large number of samples.

The parametric study of three families of parameterized shapes reveals the impact and importance of the shape on the peak magnitude of the FRF, the peak magnitude of the FRF per unit of area, and the natural frequency. Some important trends can be identified: parameter R, which characterizes the width to length ratio, is the less sensitive parameter that affects the natural frequency in absence of tip mass while the tip mass increases the sensitivity of all geometrical parameters. Additionally, it is shown that any type of geometry with or without tip mass could be tuned to the same natural frequency, however, the addition of a tip mass tends to lead to smaller devices.

In the NURBS representation of the boundary shape, locations of the control points can be optimized to achieve the best power output. The Krigging-aided optimization is carried out to explore non-conventional shapes which can improve performance of the device in certain applications. The optimization is performed in a wide design space, including configurations of various shapes and sizes, and the variable tip mass. The results are presented adopting a multi-objective optimization such that the FRF and the FRF per unit of area are simultaneously maximized for a device with a natural frequency of 30 Hz. Three tip mass configurations are tried: without tip mass, with a fixed tip mass of 0.025 kg and accounting the tip mass as an additional design variable bounded between the previous values. The maximum peak of the FRF is achieved when no tip mass is used leading to a device with large surface. On the other hand, the maximum peak of the FRF per unit of area is achieved for the highest tip mass employed, in this case leading to a small PEH with a narrow tip. When both objectives were considered, an optimal front is identified where the optimal tip mass varies from zero to its maximum value.

CRediT authorship contribution statement

P. Peralta: Conceptualization, Methodology, Software. **R.O. Ruiz:** Supervision, Conceptualization, Writing - original draft, Funding acquisition. **S. Natarajan:** Conceptualization, Validation. **E. Atroshchenko:** Conceptualization, Writing - review & editing.

Declaration of competing interest

The authors declare that they have no known competing financial interests or personal relationships that could have appeared to influence the work reported in this paper.

Acknowledgements

This research is supported by Vicerrectoría de Investigación y Desarrollo (VID) de la Universidad de Chile through the program UCH-1566 and the Comisión Nacional de Investigación Científica y Tecnológica de Chile through the project CONICYT/FONDECYT/11180812.

Appendix A. Supplementary data

Supplementary data to this article can be found online at https://doi.org/10.1016/j.jsv.2020.115521.

References

[1] Anam Khalid, Amit Kumar Redhewal, Manoj Kumar, Anupam Srivastav, Piezoelectric vibration harvesters based on vibrations of cantilevered bimorphs: a review, Mater. Sci. Appl. 6 (2015) 818–827.
[2] C. Williams, R. Yates, Analysis of a micro-electric generator for microsystems, sensors and actuators A: physical 52, in: Proceedings of the 8th International Conference on Solid-State Sensors and Actuators Eurosensors IX, 1996, pp. 8–11.
[3] N.E. dutoit, B.L. wardle, S.-G. kim, Design considerations for mems-scale piezoelectric mechanical vibration energy harvesters, Integrated Ferroelectrics Int. J. 71 (2005) 121–160.
[4] S. Roundy, P.K. Wright, J. Rabaey, A study of low level vibrations as a power source for wireless sensor nodes, Comput. Commun. 26 (2003) 1131–1144 Ubiquitous Computing.
[5] C. Wei, X. Jing, A comprehensive review on vibration energy harvesting: modelling and realization, Renew. Sustain. Energy Rev. 74 (2017) 1–18.
[6] A. Erturk, D.J. Inman, On mechanical modeling of cantilevered piezoelectric vibration energy harvesters, J. Intell. Mater. Syst. Struct. 19 (2008) 1311–1325.
[7] A. Erturk, D.J. Inman, A distributed parameter electromechanical model for cantilevered piezoelectric energy harvesters, J. Vib. Acoust. 130 (2008) 041002.
[8] A. Erturk, D.J. Inman, An experimentally validated bimorph cantilever model for piezoelectric energy harvesting from base excitations, Smart Mater. Struct. 18 (2009) 025009.
[9] C.D.M. Junior, A. Erturk, D.J. Inman, An electromechanical finite element model for piezoelectric energy harvester plates, J. Sound Vib. 327 (2009) 9–25.
[10] S. Roundy, E.S. Leland, J. Baker, E. Carleton, E. Reilly, E. Lai, B. Otis, J.M. Rabaey, P.K. Wright, V. Sundararajan, Improving power output for vibration-based energy scavengers, IEEE Perv. Comput. 4 (2005) 28–36.
[11] J. Baker, S. Roundy, P. Wright, Alternative Geometries for Increasing Power Density in Vibration Energy Scavenging for Wireless Sensor Networks, p. 5617.
[12] K. Savarimuthu, R.,M.,G. Sankararajan, M.A. Roji, Design and analysis of cantilever based piezoelectric vibration energy harvester, Circ. World 44 (2018) 78–89.
[13] D. Benasciutti, L. Moro, S. Zelenika, E. Brusa, Vibration energy scavenging via piezoelectric bimorphs of optimized shapes, Microsyst. Technol. 16 (2010) 657–668.
[14] F. Goldschmidtboeing, P. Woias, Characterization of different beam shapes for piezoelectric energy harvesting, J. Micromech. Microeng. 18 (2008).

[15] J.M. Dietl, E. Garcia, Beam shape optimization for power harvesting, J. Intell. Mater. Syst. Struct. 21 (2010) 633–646.
[16] S.B. Ayed, A. Abdelkefi, F. Najar, M.R. Hajj, Design and performance of variable-shaped piezoelectric energy harvesters, J. Intell. Mater. Syst. Struct. 25 (2014) 174–186.
[17] J. Park, S. Lee, B.M. Kwak, Design optimization of piezoelectric energy harvester subject to tip excitation, J. Mech. Sci. Technol. 26 (2012) 137–143.
[18] R. Hosseini, M. Nouri, Shape design optimization of unimorph piezoelectric cantilever energy harvester, J. Comput. Appl. Mech. 47 (2016) 247–259.
[19] J.A. Cottrell, A. Reali, Y. Bazilevs, T.J. Hughes, Isogeometric analysis of structural vibrations, Comput. Methods Appl. Mech. Eng. 195 (2006) 5257–5296.
[20] S. Shojaee, E. Izadpanah, N. Valizadeh, J. Kiendl, Free vibration analysis of thin plates by using a nurbs-based isogeometric approach, Finite Elem. Anal. Des. 61 (2012) 23–34.
[21] J. Kiendl, K.-U. Bletzinger, J. Linhard, R. Wchner, Isogeometric shell analysis with Kirchhoff-love elements, Comput. Methods Appl. Mech. Eng. 198 (2009) 3902–3914.
[22] D. Benson, Y. Bazilevs, M.-C. Hsu, T. Hughes, A large deformation, rotation-free, isogeometric shell, Comput. Methods Appl. Mech. Eng. 200 (2011) 1367–1378.
[23] E. Atroshchenko, S. Tomar, G. Xu, S.P. Bordas, Weakening the tight coupling between geometry and simulation in isogeometric analysis: from sub-and super-geometric analysis to geometry-independent field approximation (gift), Int. J. Numer. Methods Eng. 114 (2018) 1131–1159.
[24] S. Cho, S.-H. Ha, Isogeometric shape design optimization: exact geometry and enhanced sensitivity, Struct. Multidiscip. Optim. 38 (2008) 53.
[25] S. Cai, W. Zhang, J. Zhu, T. Gao, Stress constrained shape and topology optimization with fixed mesh: a b-spline finite cell method combined with level set function, Comput. Methods Appl. Mech. Eng. 278 (2014) 361–387.
[26] J. Kiendl, R. Schmidt, R. Wchner, K.-U. Bletzinger, Isogeometric shape optimization of shells using semi-analytical sensitivity analysis and sensitivity weighting, Comput. Methods Appl. Mech. Eng. 274 (2014) 148–167.
[27] D. Fueder, B. Simeon, A.-V. Vuong, Fundamental aspects of shape optimization in the context of isogeometric analysis, Comput. Methods Appl. Mech. Eng. 286 (2015) 313–331.
[28] Y. Wang, Z.-P. Wang, Z. Xia, L.-H. Poh, Structural design optimization using isogeometric analysis: a comprehensive review, Comput. Model. Eng. Sci.: Comput. Model. Eng. Sci. 117 (3) (2018) 455–507.
[29] R.O. Ruiz, V. Meruane, Uncertainties propagation and global sensitivity analysis of the frequency response function of piezoelectric energy harvesters, Smart Mater. Struct. 26 (2017) 065003.
[30] V.R. Franco, P.S. Varoto, Parameter uncertainties in the design and optimization of cantilever piezoelectric energy harvesters, Mech. Syst. Signal Process. 93 (2017) 593–609.
[31] P. Peralta, R.O. Ruiz, V. Meruane, Experimental study of the variations in the electromechanical properties of piezoelectric energy harvesters and their impact on the frequency response function, Mech. Syst. Signal Process. 115 (2019) 469–482.
[32] J. Lin, C. Scalo, L. Hesselink, High-fidelity simulation of a standing-wave thermoacousticpiezoelectric engine, J. Fluid Mech. 808 (2016) 19–60.
[33] M.-O. Kim, S. Pyo, Y. Oh, Y. Kang, K.-H. Cho, J. Choi, J. Kim, Flexible and multi-directional piezoelectric energy harvester for self-powered human motion sensor, Smart Mater. Struct. 27 (2018) 035001.
[34] H. Elahi, M. Eugeni, P. Gaudenzi, A review on mechanisms for piezoelectric-based energy harvesters, Energies 11 (2018) 1850.
[35] A. Erturk, D.J. Inman, Piezoelectric Energy Harvesting, John Wiley & Sons, 2011.
[36] S.H. Crandall, Dynamics of Mechanical and Electromechanical Systems, McGraw-Hill, 1968.
[37] T.J. Hughes, J.A. Cottrell, Y. Bazilevs, Isogeometric analysis: cad, finite elements, nurbs, exact geometry and mesh refinement, Comput. Methods Appl. Mech. Eng. 194 (2005) 4135–4195.
[38] Q. Wang, S. Quek, C. Sun, X. Liu, Analysis of piezoelectric coupled circular plate, Smart Mater. Struct. 10 (2001) 229.
[39] X. Liu, Q. Wang, S. Quek, Analytical solution for free vibration of piezoelectric coupled moderately thick circular plates, Int. J. Solid Struct. 39 (2002) 2129–2151.
[40] S. Hosseini-Hashemi, M. Eshaghi, H.R.D. Taher, An exact analytical solution for freely vibrating piezoelectric coupled circular/annular thick plates using reddy plate theory, Compos. Struct. 92 (2010) 1333–1351.
[41] C.J. Rupp, A. Evgrafov, K. Maute, M.L. Dunn, Design of piezoelectric energy harvesting systems: a topology optimization approach based on multilayer plates and shells, J. Intell. Mater. Syst. Struct. 20 (2009) 1923–1939.
[42] P. Peralta, R.O. Ruiz, A.A. Taflanidis, Bayesian identification of electromechanical properties in piezoelectric energy harvesters, Mech. Syst. Signal Process. (2020) 106506.
[43] S.N. Lophaven, H.B. Nielsen, J. Sndergaard, Dace-a Matlab Kriging Toolbox, Version 2.0, Informatics and Mathematical Modelling, 2002.
[44] M. Meckesheimer, A.J. Booker, R.R. Barton, T.W. Simpson, Computationally inexpensive metamodel assessment strategies, AIAA J. 40 (2002) 2053–2060.
[45] A. Florian, An efficient sampling scheme: updated Latin hypercube sampling, Probabilist. Eng. Mech. 7 (1992) 123–130.
[46] R.T. Marler, J.S. Arora, Survey of multi-objective optimization methods for engineering, Struct. Multidiscip. Optim. 26 (2004) 369–395.
[47] R. Ruiz, A.A. Taflanidis, D. Lopez-Garcia, C.R. Vetter, Life-cycle based design of mass dampers for the chilean region and its application for the evaluation of the effectiveness of tuned liquid dampers with floating roof, Bull. Earthq. Eng. 14 (2016) 943–970.
[48] R. Ruiz, A. Taflanidis, A. Giaralis, D. Lopez-Garcia, Risk-informed optimization of the tuned mass-damper-inerter (tmdi) for the seismic protection of multi-storey building structures, Eng. Struct. 177 (2018) 836–850.
[49] J. Zhang, A. Taflanidis, J. Medina, Sequential approximate optimization for design under uncertainty problems utilizing kriging metamodeling in augmented input space, Comput. Methods Appl. Mech. Eng. 315 (2017) 369–395.